SIGNAL TRANSDUCTION

Increased PIP3 activity blocks nanoparticle mRNA delivery

Kalina Paunovska*, Alejandro Da Silva Sanchez*, Matthew T. Foster, David Loughrey, Emmeline L. Blanchard, Fatima Z. Islam, Zubao Gan, Athanasios Mantalaris, Philip J. Santangelo, James E. Dahlman†

The biological pathways that affect drug delivery in vivo remain poorly understood. We hypothesized that altering cell metabolism with phosphatidylinositol (3,4,5)-triphosphate (PIP3), a bioactive lipid upstream of the metabolic pathway PI3K (phosphatidylinositol 3-kinase)/AKT/ mTOR (mammalian target of rapamycin) would transiently increase protein translated by nanoparticle-delivered messenger RNA (mRNA) since these pathways increase growth and proliferation. Instead, we found that PIP3 blocked delivery of clinically-relevant lipid nanoparticles (LNPs) across multiple cell types in vitro and in vivo. PIP3-driven reductions in LNP delivery were not caused by toxicity, cell uptake, or endosomal escape. Interestingly, RNA sequencing and metabolomics analyses suggested an increase in basal metabolic rate. Higher transcriptional activity and mitochondrial expansion led us to formulate two competing hypotheses that explain the reductions in LNP-mediated mRNA delivery. First, PIP3 induced consumption of limited cellular resources, "drowning out" exogenously-delivered mRNA. Second, PIP3 triggers a catabolic response that leads to protein degradation and decreased translation.

INTRODUCTION

Nanoparticle-mediated mRNA delivery has the potential to express any gene, making this approach a promising way to treat disease. Nanoparticle delivery is a multistep process governed by interactions between synthetic materials and the body. As a result, understanding the biological pathways that affect nanoparticles can enable scientists to design effective drug delivery systems. For example, serum proteins adsorbed onto nanoparticles can promote or, alternatively, block interactions between nanoparticles and cell surface receptors (*1*–*3*). In one case, the expression of apolipoprotein E was necessary for ionizable lipid nanoparticles (LNPs) to deliver small interfering RNA (siRNA) to hepatocytes in vivo; this was mediated by the low-density lipoprotein receptor, which is expressed on the cell surface (*4*). Understanding this biological mechanism of action helped lead to the development of a U.S. Food and Drug Administration (FDA)–approved LNP (*5*). It is similarly accepted that once a nanoparticle reaches a cell, the route by which it accesses the cytoplasm affects its activity. For example, studies manipulating endocytosis with small molecules (*6*–*8*), siRNA (*9*, *10*), CRISPR-Cas9 (*6*), or knockout mice (*11*, *12*) have revealed that nanoparticle endocytosis and endosomal escape are carefully regulated. In one representative example, researchers found that LNPs containing siRNA engage both clathrin-mediated endocytosis and macropinocytosis to deliver their cargo. The bioavailability of the siRNA was limited by the escape of the drug from hybrid endosomes, which exhibited early and late endosomal characteristics (*9*). The researchers also characterized the escape window for siRNAs and estimate that only 1 to 2% of administered siRNAs enter the cytosol. In another example, researchers found that less than 1% of mRNAs delivered by LNPs made it to the cytosol of a cell and that mRNA endosomal escape was highly dependent on LNP structure (*13*).

Wallace H. Coulter Department of Biomedical Engineering, Georgia Institute of Technology, Atlanta, GA 30332, USA.
*These authors contributed equally to this work.
†Corresponding author. Email: james.dahlman@bme.gatech.edu

In this study, we sought to answer whether cell metabolism alters nanoparticle delivery. We focused on this question for four reasons. First, it has immediate clinical relevance; nanomedicines are administered to patients with disorders characterized by strong metabolic phenotypes, including cancer (*14*). Second, literature suggests that metabolism could affect some steps of the drug delivery process. Specifically, to achieve cytoplasmic mRNA delivery, a nanoparticle first interacts with serum proteins and the cell surface. Metabolism influences how cells interact with lipoproteins (*15*), which are naturally occurring nanomaterials that can have a similar chemical structure to LNPs (*12*, *16*). After a nanoparticle reaches the cell, it can enter and, with less frequency, exit an endosome; metabolism affects endocytosis pathways important for nanomedicine (*17*). Third, mRNA that enters the cytoplasm must be translated into protein; cell metabolism affects mRNA translation and degradation (*18*). Last, recent evidence implicates mammalian target of rapamycin (mTOR), a canonical metabolic pathway, as a mediator and player in both antisense oligonucleotide activity (*19*) and nanoparticle delivery via to-be-determined mechanisms (*6*). In the first example, the authors found that small-molecule inhibition of mTOR increased antisense oligonucleotide activity in vivo. In the second example, the authors inactivated genes related to endocytosis using CRISPR. They found that knocking out Rab7a, which is necessary for late endosomal trafficking, reduced delivery, whereas knocking out Rab4a and Rab5a, which is necessary for endosomal recycling and early endosomal trafficking, respectively, did not. The authors reasoned that halting endosomal maturation by deleting Rab7a blocked the metabolic gene *mTORC1*, which is expressed on the lysosomal surface, from initiating mRNA translation. To verify this, the authors activated *mTORC1* and observed increased protein expression.

These lines of evidence led us to reason that we could manipulate metabolism with small molecules to improve LNP delivery. Specifically, we hypothesized that it was possible to metabolically reprogram cells so that more mRNA was translated once it reached the cytoplasm. To achieve this goal, we chose the bioactive lipid phosphatidylinositol (3,4,5)-triphosphate (PIP3). PIP3, a membrane

phospholipid created by the phosphorylation of PIP2, mediated by phosphatidylinositol 3-kinase (PI3K), signals via interactions with proteins containing pleckstrin homology domains at the plasma membrane (*20*). Specifically, PIP3 binds to phosphoinositide-dependent kinase 1, initiating the kinase to phosphorylate and activate Akt. Phosphorylation of Akt leads to inhibition of the TSC (tuberous sclerosis complex) complex and downstream activation of Rheb, which stimulates mTORC1 kinase activity (*21*, *22*). Increased PIP3 concentrations up-regulate clathrin- and dynamin-mediated endocytosis of epidermal growth factor receptor (*23*) and sort endosomal cargos in epithelial cells (*24*), suggesting that PIP3 could increase endocytosis. Increased PIP3 activity also promotes cell growth via several mechanisms, including increased translation (*25*). We therefore reasoned that treating cells with PIP3 and mRNA-containing LNPs would transiently up-regulate translation, thereby increasing the "effective potency" of the LNPs. However, our data did not support this hypothesis. We found the opposite: PIP3 potently blocked mRNA delivery mediated by three clinically relevant (FDA-approved or licensed for clinical translation) LNPs (Fig. 1A). By performing RNA sequencing (RNA-seq) and metabolomics analyses of PIP3-treated cells, we identified pathways that have not previously been related to LNP delivery. Our analysis suggests two competing hypotheses. First, PIP3 increases endogenous transcription, which may reduce the effective concentration of exogenous mRNA delivered by the LNPs. Second, increases in basal metabolic rate may trigger a catabolic phenotype that leads to protein degradation and decreased translation. These data highlight the importance of understanding the metabolic profile of target and off-target cells when designing nanomedicines.

RESULTS

PIP3 treatment reduces mRNA translation in multiple cell types

To study how PIP3 affected LNP-mediated mRNA delivery, we used microfluidics (*26*) to formulate a clinically relevant LNP (herein named LNP1) so that it carried chemically modified mRNA encoding green fluorescent protein (GFP) (Fig. 1B and fig. S1A). LNP1 has delivered mRNA to lung endothelial cells in vivo (*27*) and is composed of the lipid **cKK-E12**, which delivered RNA in non-human primates (NHPs) (*28*). We used two cell lines: human

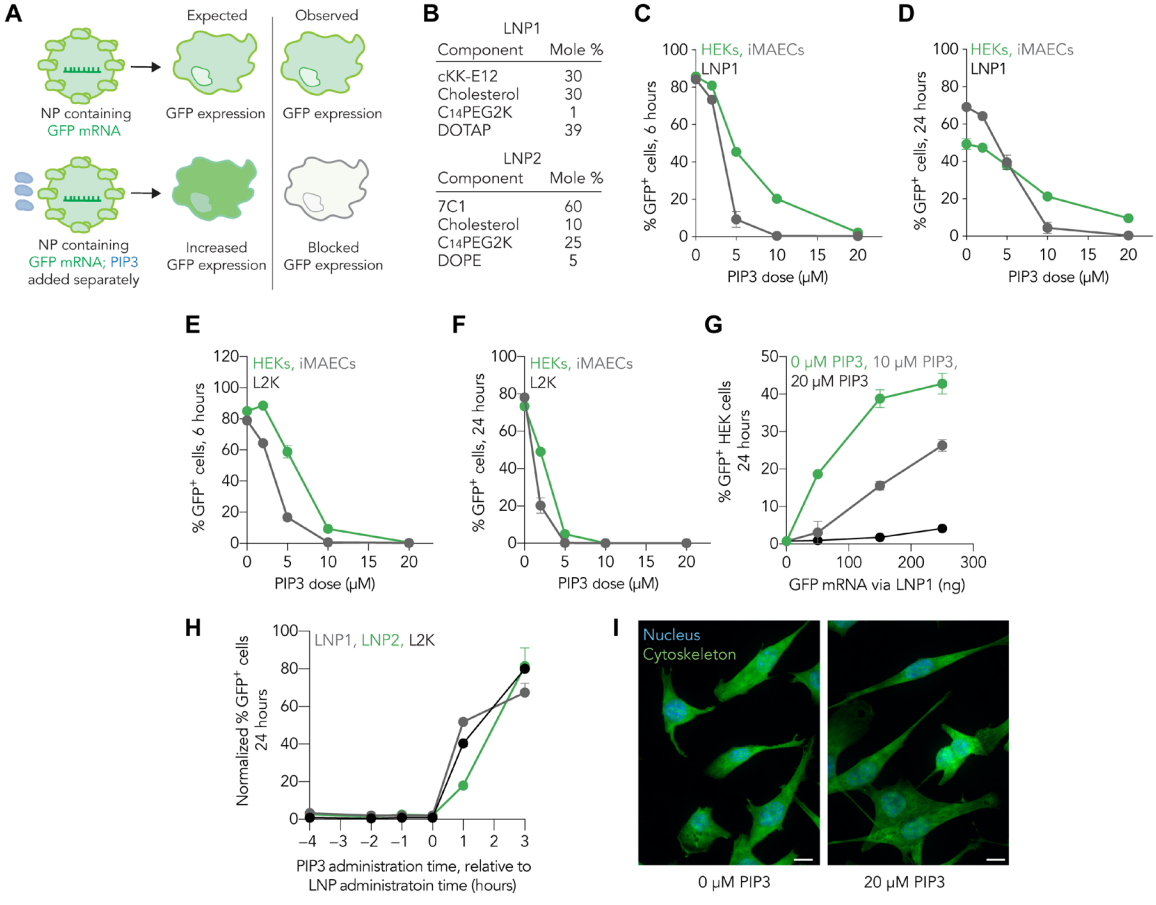

Fig. 1. PIP3 reduces nanoparticle-mediated mRNA delivery in vitro. (**A**) PIP3 blocks the functional delivery of nanoparticles (NP) carrying GFP mRNA. The data suggest that this is driven in part by reduced endosomal escape. (**B**) LNP1 and LNP2 chemical composition. Concurrent delivery of PIP3 and 50 ng of LNP1 carrying GFP mRNA led to decreased GFP expression in cells (**C**) Six hours and (**D**) 24 hours after transfection. Reduced GFP expression was also observed at (**E**) 6 hours and (**F**) 24 hours when mRNA was carried by L2K and administered at a dose of 400 ng per well. (**G**) Concurrent delivery of PIP3 and varying doses of LNP1 carrying GFP mRNA shows that the percentage of GFP^+ cells decreases as the amount of PIP3 increases. (**H**) PIP3 administered before, concurrently, or after 50 ng of LNP1, 150 ng of LNP2, and 400 ng of L2K carrying GFP mRNA leads to a decrease in GFP expression. (**I**) PIP3 did not lead to changes in iMAEC cell morphology 24 hours after PIP3 administration. Scale bars, 10 μm. Nuclei stained with DAPI and cytoskeleton (phalloidin) stained with GFP.

embryonic kidney (HEKs) and immortalized murine aortic endothelial cells (iMAECs) (*29*). Cells in 24-well plates were concurrently treated with GFP mRNA and PIP3. Six or 24 hours later, we quantified mRNA delivery by measuring the percentage of GFP^+ cells via flow cytometry, using untreated cells as controls (fig. S1, B to J). We observed a PIP3 dose-dependent decrease in GFP fluorescence (Fig. 1, C and D). This effect was statistically significant: At 6 hours, GFP expression was reduced from 85% (0 μM PIP3) to 0% (10 μM PIP3) in iMAECs and from 85% (0 μM PIP3) to 20% (10 μM PIP3) in HEKs (Fig. 1C). We repeated the experiment using Lipofectamine 2000 (L2K) and observed a similar PIP3 dose-dependent reduction in GFP expression from 80 to 85% (0 μM PIP3) to 0 to 10% (10 μM PIP3) in both iMAECs and HEKs at 6 and 24 hours (Fig. 1, E and F). We repeated the experiment with a second clinically relevant LNP (*30*) (termed LNP2) that has a different chemical structure and in vivo tropism from LNP1 (Fig. 1B). LNP2 delivers mRNA to splenic endothelial cells in vivo (*30*) and consists of the lipid 7C1 (*31*) (fig. S1A), which delivered RNA in NHPs (*32*) and is licensed for clinical development. We observed PIP3 dose-dependent inhibition of GFP fluorescence after LNP2 transfection (fig. S1, Q and R). We then treated cells with 0, 10, or 20 μM PIP3 and concurrently administered increasing doses of GFP mRNA. GFP expression decreased with PIP3 dose and increased with GFP mRNA dose (Fig. 1G and fig. S1, S and T). Statistical significances of these results are all listed (fig. S1, K to P). To understand the kinetics of this effect, we then varied the timing between PIP3 and LNP treatment. PIP3-treated cells expressed less GFP when PIP3 was administered 4 hours before the LNP and expressed normal levels of GFP when PIP3 was administered 3 hours after the LNPs (Fig. 1H). These results led us to conclude that treating cells with PIP3 reduced the amount of mRNA translated into protein after LNP delivery in vitro.

Reduced protein expression is not caused by overt toxicity

We reasoned that this reduction in mRNA delivery could be due to overt cellular toxicity or inflammation (*33*). We performed four assays comparing untreated cells to PIP3-treated cells: (i) MTT (6 or 24 hours after PIP3 administration), (ii) lactate dehydrogenase (LDH) (24 hours after PIP3 administration), (iii) nuclear factor κB (NF-κB) activation (8 or 12 hours after PIP3 administration), and (iv) cell morphology (6 or 24 hours after PIP3 administration). We did not find any evidence of toxicity. Specifically, we found no significant change in MTT readouts when administering PIP3 at a 10 or 20 μM dose (fig. S1U) and no significant decrease in LDH readouts after PIP3 was administered to cells at 10 or 20 μM; the positive control lipopolysaccharide (LPS) did reduce cell viability (fig. S1V). Similarly, PIP3 did not increase NF-κB activation in NF-κB reporter cells (fig. S1W). We then analyzed the effect of PIP3 on iMAEC cell morphology and found no difference between untreated cells and cells treated with PIP3 (Fig. 1I). Last, we performed a literature search and found that 25 μM PIP3 doses did not cause toxicity (*34*). These data did not support our hypothesis that reduced protein expression was due to overt cytotoxicity.

Reduced protein production is not explained by cell uptake or endosomal escape

Our second hypothesis was that PIP3 blocked mRNA delivery by changing (i) particle stability, (ii) cell uptake, (iii) endosomal escape, or (iv) a combination thereof (Fig. 2A). To study (i) particle stability, we quantified the Z-average hydrodynamic diameter of LNP1 in phosphate-buffered saline (PBS) supplemented with mouse serum or iMAEC media using dynamic light scattering. Adding PIP3 did not change LNP diameter (fig. S2A). To study (ii) cell uptake, we formulated LNP1 carrying GFP mRNA so that it contained the phospholipid DOTAP (1,2-dioleoyl-3-trimethylammonium-propane) labeled with a fluorescent probe (NBD-DOTAP) (λ_{abs} = 460 nm; λ_{em} = 535 nm). Separately, we formulated LNP2 carrying mRNA so that it contained Alexa Fluor 647–tagged DOPE (1,2-dioleoyl-sn-glycero-3-phosphoethanolamine) (AF647-DOPE) (λ_{ex} = 643 nm; λ_{em} = 662 nm). We did not change formulation ratios; we replaced normal DOTAP and DOPE with fluorescent DOTAP and DOPE. We administered the LNPs to HEKs and iMAECs at a dose of 50 ng per well for LNP1 and 150 ng per well for LNP2. We then isolated cells and quantified cellular fluorescence. As a negative control, we used untreated cells. PIP3 did not affect LNP1 uptake in iMAECs (Fig. 2B) but did affect LNP1 uptake in HEKs at early time points; there was a 6% increase in LNP uptake in PIP3-treated HEKs at both 0.5 and 1 hour (Fig. 2C). PIP3 increased LNP2 uptake in iMAECs by 52% at 2 hours, 56% at 6 hours, and 29% at 24 hours (Fig. 2D) and decreased LNP2 uptake in HEKs by 72% at 2 hours (Fig. 2E). These data suggested that PIP3 may alter nanoparticle uptake; however, the effects were not conserved across LNPs or cell types. Changes to LNP uptake were far less substantial than the (almost total) reduction in GFP mean fluorescence intensity (MFI). We therefore concluded that these effects on LNP uptake were not sufficient to fully explain the decrease in protein production.

We then investigated whether PIP3 reduced canonical endocytosis using two pathways: clathrin- and caveolin-mediated endocytoses. We quantified the uptake of transferrin and cholera toxin B, which are ligands for clathrin- and caveolin-mediated endocytoses, respectively (*35*, *36*). We treated cells with PIP3 and fluorescently tagged transferrin or cholera toxin B. Compared to cells that were not pretreated with PIP3, transferrin and cholera toxin B uptake was unchanged in iMAECs and HEKs (fig. S2, B and C). These data led us to conclude that PIP3 did not substantially affect canonical clathrin- or caveolin-mediated endocytosis.

We then studied (iii) whether PIP3 reduced LNP endosomal escape. We focused on LNP2, since its uptake was affected more by PIP3 than LNP1. We treated cells with LNP2 formulated with fluorescently labeled DOPE. Thirty minutes and 6 hours after delivery, cells were fixed and stained with 1° antibodies against Rab7, early endosome antigen 1 (EEA1), and CD63, which mark different stages of endosomal maturation (*37*). We then used a 2° antibody to stain all endosomes (Fig. 2F) and quantified both the line profiles (Fig. 2, G and H) and the M1 and M2 coefficients of LNPs with endosomes for 30 cells per treatment condition as previously described (*37*) (Fig. 2, I and J). The M1 coefficient quantifies the fraction of LNP signal that is colocalized with endosomal signal, while the M2 coefficient quantifies the fraction of endosomal signal that is colocalized with LNP signal. Thus, a lower M1 coefficient indicates greater endosomal escape of LNP in the cell at that time point. Cells treated with both LNP and PIP3 had 49 and 27% lower M1 coefficients than cells treated with LNP only at 30 min and 6 hours, respectively (Fig. 2I). Cells treated with both LNP and PIP3 also had a 7.6-fold reduction in M2 coefficient at 6 hours compared to those treated with LNP only (Fig. 2J). The decrease in the M1 coefficients after PIP3 treatment indicates that, at the tested time points, PIP3 increased the endosomal escape of LNPs. However,

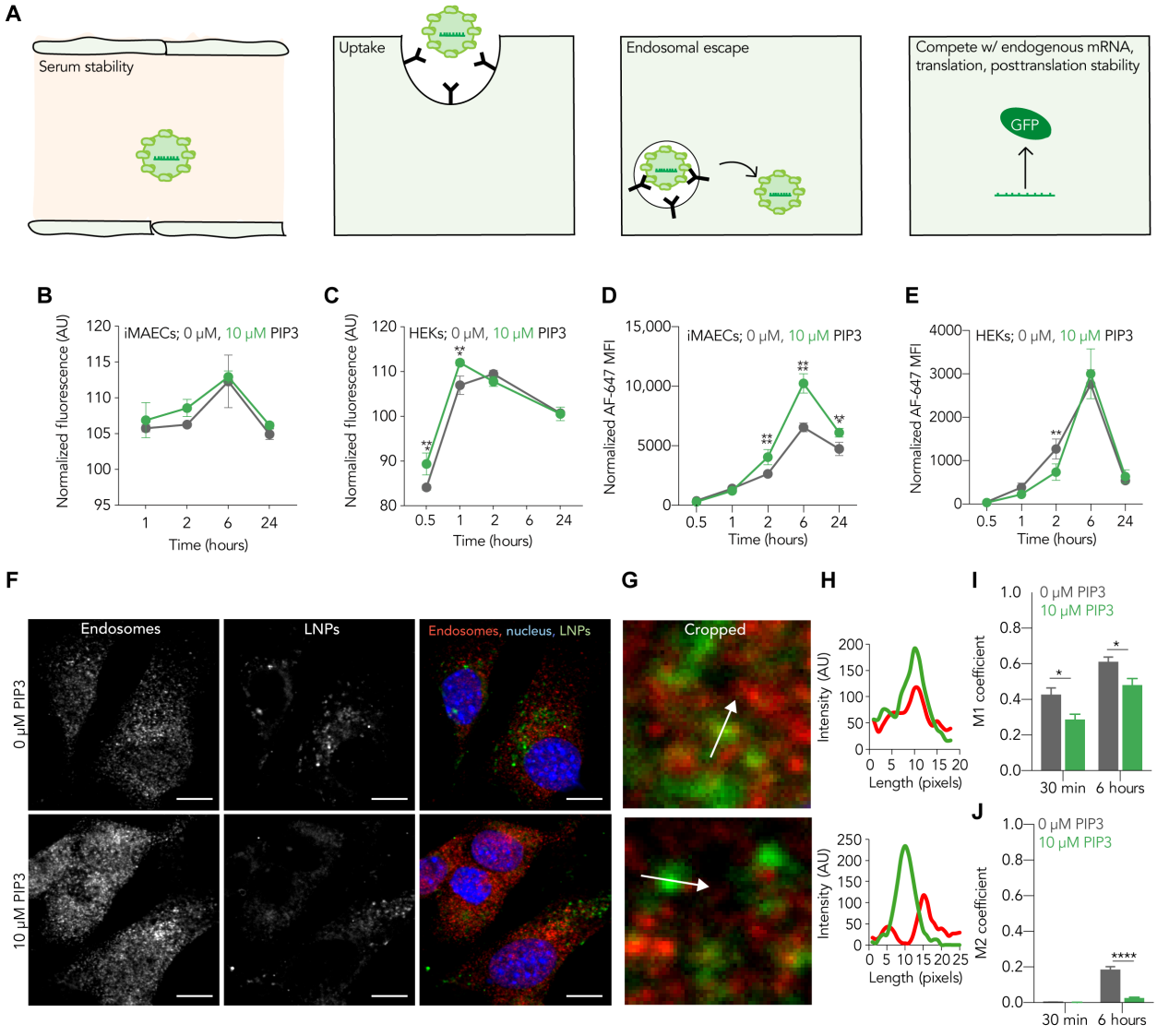

Fig. 2. Analysis of the effects PIP3 has on LNP uptake and endosomal escape. (**A**) We reasoned that PIP3 could reduce LNP delivery by reducing LNP serum stability, inhibiting cell uptake or endosomal escape, or by altering the metabolic state of the cell. (**B** to **E**) LNPs containing GFP mRNA were formulated with fluorescent phospholipids and administered to cells. Cell normalized fluorescence was determined relative to an untreated control at each time point. Normalized fluorescence did not change over time in (B) iMAECs and did change slightly in (C) HEKs after administration of LNP1 and PIP3. Similarly, PIP3 had a minimal effect on LNP2 uptake, measured by MFI, in either (D) iMAECs or (E) HEKs. Normalized AF-647 MFI was also determined relative to an untreated control at each time point. *P < 0.0332, **P < 0.0021, ***P < 0.0002, and ****P < 0.0001. (**F**) In cells treated with PIP3, LNPs (red) colocalize with endosomes (green), whereas the opposite is observed without PIP3. (**G**) Colocalization images of endosomes and LNPs can be used to draw (**H**) representative line profiles. (**I**) The M1 coefficient shows a significant difference in colocalization of LNP and endosome for cells treated with PIP3 after 30 min and 6 hours. (**J**) The M2 coefficient is low, indicating that, as expected, there are more endosomes than endosomes colocalized with LNPs. All microscopy images are shown with 10-μm scale bars. Although only a few representative cells are shown, the M1/M2 coefficient generation represents colocalization analysis of more than 30 cells per condition. AU, arbitrary units.

these data do not explain the absence of GFP expression in PIP3-treated cells. Although we cannot discard potential interplay between endosomal trafficking and cell metabolism mediated by PIP3, these results suggest that endosomal escape does not explain the observed effect.

RNA-seq and metabolomics suggest pathways that could influence LNP delivery

The data above led us to conclude that our second hypothesis did not explain the robust reduction in mRNA delivery. We therefore tested a third hypothesis: that cell metabolism altered LNP delivery (Fig. 2A). To test this, we used RNA-seq analysis in iMAECs that were not treated with PIP3, as well as cells treated with 10 μM PIP3 for 6 or 24 hours. We generated a total of 530 million clean reads from 12 complementary DNA (cDNA) libraries using Illumina NextSeq, an average of 114.4× fold coverage of the coding region of the genome. We found that more than 95% of the total reads were uniquely mapped to the reference genome.

We generated two volcano plots (6 and 24 hours) to analyze the adjusted P value as well as the fold change of each transcript, relative to the untreated cells (Fig. 3, A and B). Specifically, we set a $P < 0.05$ and fold change >1.5 as thresholds for differentially expressed genes.

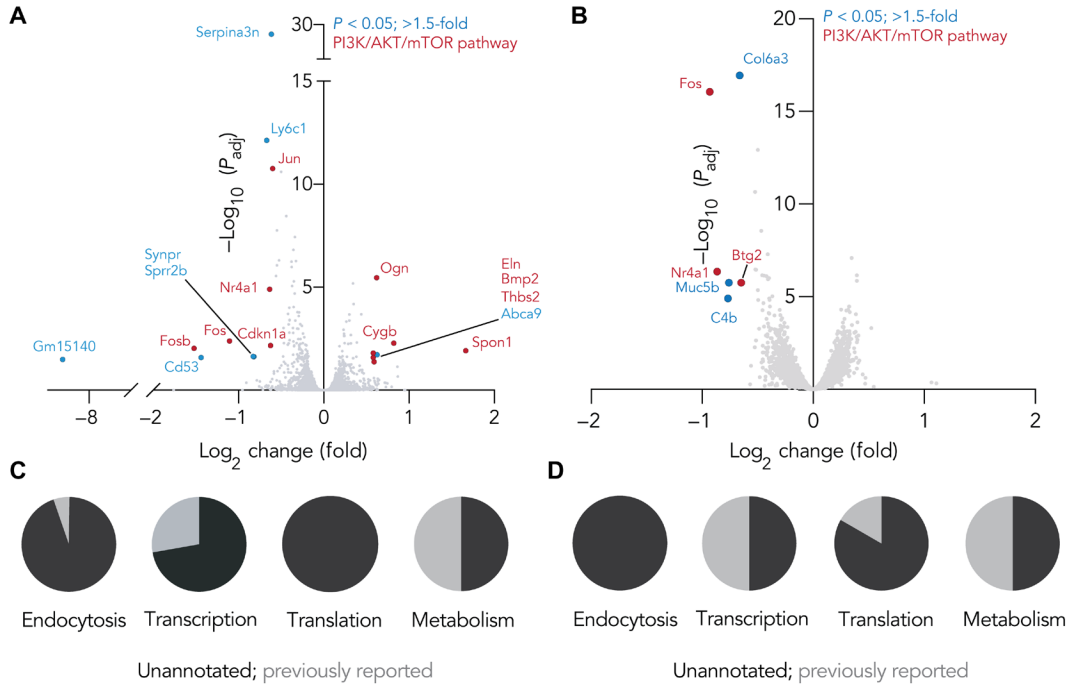

Fig. 3. PIP3 changes the transcriptional profile of a cell. More genes are up-regulated/down-regulated (**A**) 6 hours after PIP3 administration than (**B**) 24 hours after PIP3 administration. Most perturbed genes were unannotated; however, there was a noticeable change in genes associated with metabolism both (**C**) 6 hours and (**D**) 24 hours after PIP3 administration. P_{adj}, adjusted *P* value.

These data were interesting for several reasons. First, the volcano plots showed that cells were generally more perturbed 6 hours after PIP3 treatment (Fig. 3A and fig. S3, A and B) relative to 24 hours (Fig. 3B and fig. S3, C and D). When we analyzed the differentially expressed genes at the 6-hour time point, we found 7 up-regulated and 11 down-regulated genes following PIP3 exposure. At the 24-hour time point, zero genes were up-regulated and six were down-regulated. Almost none of these genes had currently annotated roles in endocytosis or translation. We believe that these genes are candidates for future LNP delivery studies.

Given that most of our identified genes were not related to pathways that "traditionally" (e.g., endocytosis) alter nanoparticle delivery, we performed a less biased analysis of the genes using the Kyoto Encyclopedia of Genes and Genomes (KEGG) analytical tool. In the 6-hour dataset, we found that the PI3K-Akt pathway was affected by PIP3 treatment (56% of the significantly differentially regulated genes); this is consistent with canonical PI3K-Akt-mTOR signaling. Signaling pathways related to immune response [interleukin-17 (IL-17)], proliferation/migration [mitogen-activated protein kinase (MAPK)], endocrine signaling, and differentiation regulated by immune response were also altered. We were unable to find previous studies relating these genes to LNP delivery in vivo. However, single-cell RNA-seq recently revealed that IL-17 regulates the immune response to tissue engineering constructs (*38*). Our data further support the hypothesis that IL-17 may regulate the biological response to synthetic materials. It was also recently shown that IL-17 production could be positively regulated through activation of RAR-related orphan receptor γ and aryl hydrocarbon receptor, both of which are regulated by the mTOR pathway (*39*, *40*). In addition, IL-17 is positively regulated by mTORC1 signaling through proteins such as STAT3 (signal transducer and activator of transcription 3) and HIF-1α (hypoxia-inducible factor 1α) (*41*). These studies provide additional evidence that IL-17 and mTOR pathways interact. Notably, 24 hours after PIP3 exposure, PI3K-Akt (50% of the significantly differentially regulated genes), MAPK, and IL-17 pathways were again differentially expressed.

We then performed a second, complementary unbiased analysis of our RNA-seq dataset. Specifically, we used Gene Ontology (GO) enrichment (specifically, the Enrichr package) to identify cellular processes regulated by the dysregulated genes we identified. We focused on GO pathways related to cellular components, biological processes, and molecular functions. In the 6-hour dataset, the GO categories for transcriptional repressor activity, RNA polymerase II activating transcription factor binding (GO:0098811), the regulation of primary microRNA transcription from RNA polymerase II promoter (GO:1902895), and RNA polymerase II transcription factor complex formation (GO:0090575) were strongly regulated (fig. S3E). After 24 hours, negative regulation of cell cycle (GO:0045786) and RNA polymerase II core promoter proximal region sequence-specific DNA binding (GO:0000978) were regulated (fig. S3F). Together, these three analyses (PubMed, KEGG, and GO) suggested that a combination of cell metabolism, transcription, and cell cycle may regulate the efficacy of mRNA delivered by LNPs.

Endocytosis and endosomal escape–based pathways and processes were not implicated at the 6- or 24-hour RNA-seq time points using the three analyses described above. Of the 18 differentially regulated genes at 6 hours, only one, thrombospondin-2 (Thbs2), has been characterized as playing a role in endocytosis (Fig. 3C) (*42*). At 24 hours, no genes are implicated in endocytosis or endosomal escape (Fig. 3D). These data support the conclusion that alteration of endocytic pathways may not drive diminished GFP protein expression after PIP3 treatment.

On the basis of these RNA analyses as well as the canonical role PIP3 has in regulating cell metabolism, we performed an unbiased metabolomic analysis of cells treated with 10 μM PIP3. In this case, we compared five groups of iMAECs: 0 hours without PIP3, 6 hours with and without PIP3, and 24 hours with and without PIP3. We used five samples per group: four for analysis and one as a control for DNA quantification. We then performed a series of analyses to ensure that the data were robust. First, we performed principal components analysis (PCA) on cells treated with or without PIP3 for 24 hours. Control cells that were not treated with PIP3 tended to have less variability across both components, while cells treated with PIP3 had little variability across PC1, which makes up for most of the variance, but displayed more variability across PC2 (Fig. 4A). We then performed hierarchical clustering, which confirmed that cells separated into two clusters; specifically, the PIP3-treated cells formed a distinct cluster, while the untreated cells clustered separately (Fig. 4B). PCA and hierarchical clustering were also performed for metabolites analyzed at 6 hours (fig. S4).

This analysis identified metabolites that were significantly changed in cells treated with PIP3, relative to time-matched cells that were not (Fig. 4C). Within the group of metabolites up-regulated at both 6 and 24 hours, we found pathways responsible for (i) anabolic metabolism with increased glycolysis, (ii) pentose phosphate regulation, (iii) methionine-enabled methyl transferase epigenetic regulation, (iv) phospholipid/glycerolipid synthesis, and (v) nucleotide synthesis. We were especially interested in (iv) and (v), which could potentially alter the stability of (iv) LNP components or (v) mRNA, respectively. Last, we found that several amino acids (specifically, isoleucine, alanine, β-alanine, homoserine, and ornithine) were significantly decreased at the 24-hour time point in PIP3-treated cells.

Both the transcriptomic and metabolomic data suggested that PIP3 led to an increase in basal metabolic rate (*43*). We therefore considered two hypotheses: (i) An increase in transcriptional and translational activity consumes limited cellular resources and "drowns out" exogenously delivered mRNA, or (ii) PIP3 triggers a catabolic response, causing protein degradation and decreased translation (*44*).

To test the first hypothesis, we administered 0 or 10 μM PIP3 to iMAECs. Twenty-four hours later, we isolated RNA from both groups, measured the total RNA concentration of the lysate, and normalized it to the number of cells. Total RNA in PIP3-treated cells increased by 19.9% relative to control cells, although the difference was not significant ($P < 0.15$) (fig. S5). These data were supported by several additional lines of evidence that suggest an increase in transcriptional

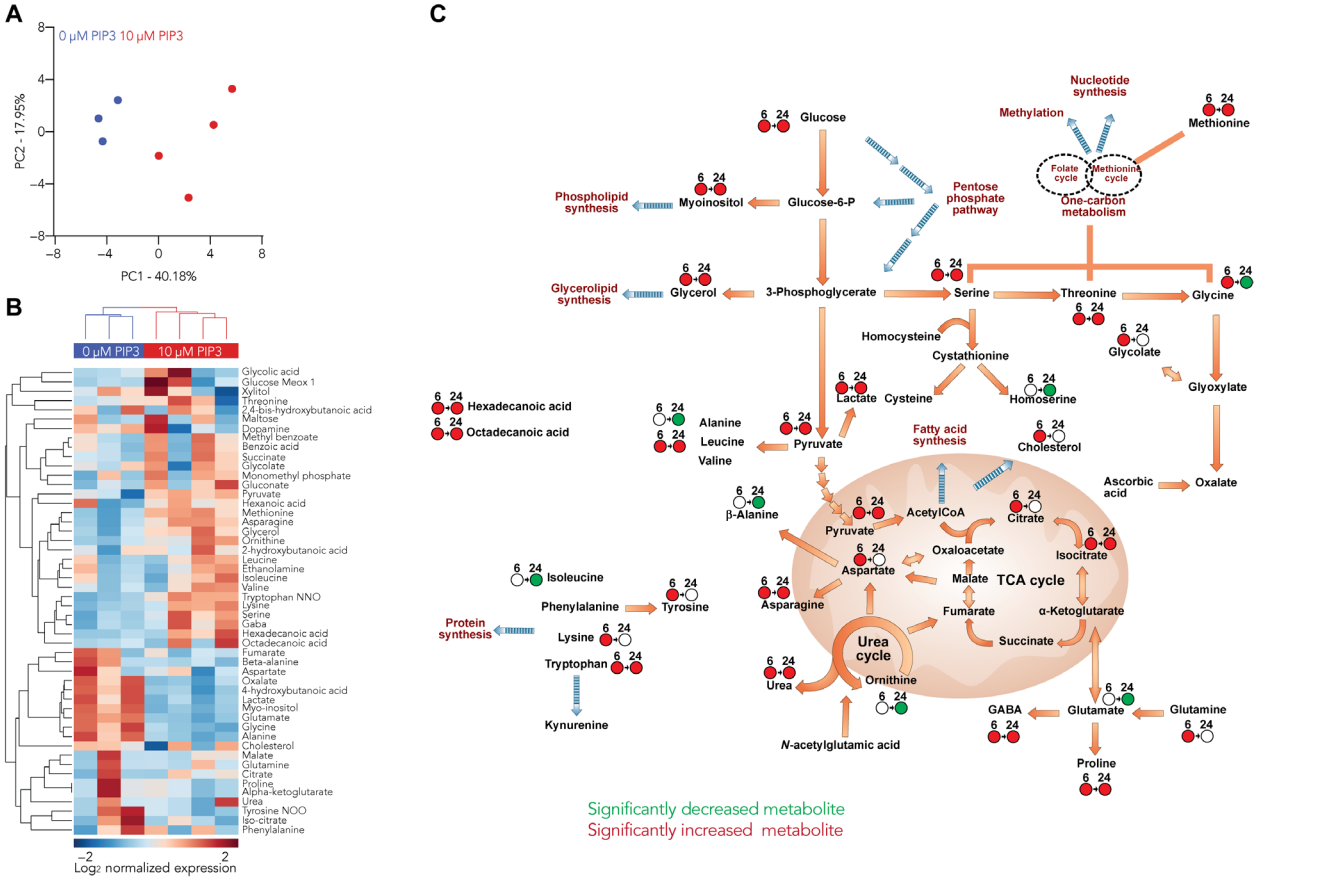

Fig. 4. PIP3 changes the metabolic state of the cell. (**A**) PCA revealed distinct grouping between cells 24 hours after they were treated with PIP3 or not treated with PIP3. Similar distinctions between treated and untreated cells at 24 hours were found using (**B**) joint hierarchical clustering, in this case, displaying metabolites across the seven samples. Significance analysis identified metabolites that were then mapped upon a (**C**) metabolic pathway diagram, highlighting significantly up-regulated and down-regulated metabolites in the PIP3-positive group compared to the PIP3-negative control at both 6 and 24 hours. Common metabolic pathways in human metabolism are shown, with orange arrows representing multi-reaction steps in these pathways; maroon labels such as "protein synthesis" represent additional cellular metabolic pathways and phenotypes significantly influenced from the canonical metabolites and pathways listed.

activity. First, several genes identified by RNA-seq regulate transcription (Fig. 3 and fig. S3, A to D). Second, the metabolic data suggested increased lipid and nucleotide synthesis (Fig. 4C). Last, 24 hours after PIP3 treatment, the number of available amino acids decreased.

To study the second hypothesis, we analyzed our metabolomics and transcriptomics data. We observed increased flux throughout glycolysis in the cytosol and tricarboxylic acid (TCA) cycle within the mitochondria (Fig. 4C), as well as up-regulation of the lipids hexa- and octadecanoic acids at 6 and 24 hours. The increase in glycolysis was characterized by expected up-regulation in amino acid synthesis, protein synthesis, and cholesterol production at 6 hours (Fig. 4C and fig. S4B) (*45*).

TCA and oxidative phosphorylation (OxPhos) are mitochondria-mediated metabolic pathways linked to glycolysis increase. Furthermore, both pathways use hexa- and octadecanoic acid (*46*). Reactive oxygen species (ROS) concentration is directly linked to mitochondrial activity in cells (*47*). PIP3-driven signaling increases mitochondrial expansion and OxPhos, suggesting an elevation of intracellular ROS levels that could shift cells to catabolism by 24 hours. This conclusion is further supported by our transcriptomic data showing changes in Fos (Fig. 3, A and B), which senses ROS stress (*48*). In addition, the reduced aspartate and TCA cycle compounds (e.g., citrate) serve as another indication of the catabolic shift described. Last, up-regulated OxPhos is a metabolic phenotype for prosurvival pathway activation, such as the differentially regulated MAPK and IL-17 pathways in the RNA-seq data (*49*).

In vivo delivery is blocked by PIP3

All the studies described above were performed in vitro, which can be a poor predictor of in vivo delivery (*50*). We therefore investigated whether PIP3 blocked LNP delivery in vivo. We performed these studies in Ai14 mice, which have a Lox-Stop-Lox-tdTomato construct under the control of a constitutive promoter. When Cre protein is produced, it translocates into the nucleus and excises the "Stop" from genomic DNA; the cells then become tdTomato$^+$ (Fig. 5A). The percentage of tdTomato$^+$ cells after Cre mRNA delivery is a validated readout of nanoparticle delivery (*27*, *30*, *51*). To quantify how PIP3 treatment altered mRNA delivery in vivo, we intravenously injected mice with PBS or PIP3 (10 mg/kg). Immediately afterwards, we intravenously injected mice with Cre mRNA (1 mg/kg) formulated inside LNP1 or LNP2. Three days later, we quantified the percentage of tdTomato$^+$ cells using flow cytometry. As a control, we gated on an Ai14 mouse treated with PBS. As previously reported, LNP1 delivered Cre mRNA to lung endothelial cells (Fig. 5B), and LNP2 delivered Cre mRNA to splenic endothelial cells (Fig. 5C). LNP1 and LNP2 did not efficiently deliver mRNA to cells in the liver (fig. S6, H to K and S to V). Thus, to evaluate whether PIP3 blocked mRNA translation in the liver, which is an important clinical target for RNA therapies, we formulated LNP3 (Fig. 5D). As reported, LNP3 delivered RNA to hepatocytes (Fig. 5E) (*28*). mRNA delivery mediated by LNP1, LNP2, and LNP3 was reduced robustly in mice treated with PIP3. Specifically, we observed a 10.4-fold reduction in tdTomato$^+$ cells when administering LNP1 and PIP3 concurrently (Fig. 5B), a 6.2-fold reduction when administering LNP2 and PIP3 concurrently (Fig. 5C), and a 13.6-fold reduction when administering LNP3 and PIP3 concurrently (Fig. 5E). In every cell type with high levels of delivery, we observed decreases in Cre mRNA delivery, most of which were statistically significant (fig. S6). None of the mice treated with PIP3 exhibited weight loss (fig. S7) or changes in behavior suggesting toxicity.

DISCUSSION

Together, these data demonstrate that the bioactive lipid PIP3 reduced the efficacy with which chemically distinct LNPs delivered mRNA in vitro and in vivo. We concluded that this effect was not driven by overt toxicity, differences in cell uptake, or endosomal escape. Instead, we found that this effect was largely driven by changes to the metabolome and transcriptome.

By performing RNA-seq and metabolic analyses, we were able to generate two hypotheses. In our first hypothesis, we proposed that exogenous LNP-delivered mRNA competes with endogenous mRNA for cellular resources that facilitate protein production. The addition of PIP3 leads to an increase in cell basal metabolic activity at the time of LNP delivery, limiting the resources available to process and effectively "drowning out" exogenously administered mRNA. This hypothesis is in its early stages; however, it is supported by several lines of evidence including (i) a 19.9% increase in cellular RNA levels, (ii) differential regulation in genes related to transcription, (iii) increases in lipid and nucleotide synthesis, and (iv) decreases in amino acid availability, all occurring 24 hours after PIP3 treatment.

Our second hypothesis is that high cell metabolic activity leads to cell stress and eventually catabolism; this catabolism degrades protein translated from mRNA (*44*). By 24 hours, we observed a ROS-driven catabolic phenotype, characterized by no significant changes in protein synthesis or cholesterol production and by significant decreases in amino acids (Fig. 4C). At 24 hours, it is feasible that

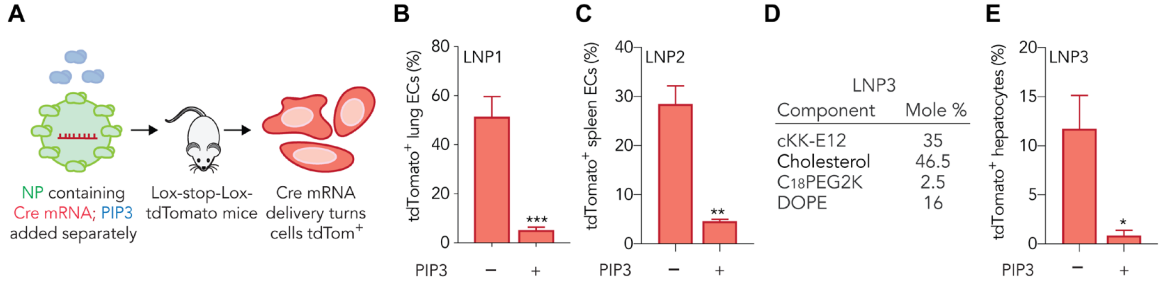

Fig. 5. PIP3 reduces LNP mRNA delivery in vivo. (**A**) Ai14 mice were injected with PIP3 (10 mg/kg) and then immediately injected with LNP carrying Cre mRNA (1 mg/kg). PIP3 consistently blocks functional LNP1 delivery in (**B**) lung endothelial cells (ECs) and functional LNP2 delivery in (**C**) splenic endothelial cells. (**D**) LNP3 was formulated to deliver Cre mRNA at 0.3 mg/kg. (**E**) PIP3 blocked LNP-mediated delivery of Cre mRNA to hepatocytes. Statistical analyses are done comparing the positive control (LNP only) to the treatment group (LNP + PIP3) using an unpaired *t* test. **P* < 0.0332, ***P* < 0.0021, and ****P* < 0.0002.

catabolic metabolism is complemented by increased autophagy, a process in which amino acids and cell surface and cytosolic proteins are endocytosed (if needed) and degraded to constituent molecules (*52*, *53*). Transcriptomics showed significant changes in Muc5b at 24 hours, which complement the changes in Fos; both genes are linked to membrane trafficking, which changes during autophagy (*54*). These data combined could potentially explain the reduction in endogenous amino acid levels at 24 hours.

We believe that these data are important for pragmatic reasons. The first LNP-based RNA drug was approved by the FDA in 2018 (*5*); its translation was aided by studies that identified the mechanism of action by which the LNP targeted hepatocytes (*4*). Second-generation RNA therapies, which also target hepatocytes, have shown promise in clinical trials (*55*). Once again, the delivery mechanism of action is understood (*56*–*58*). To continue realizing the potential of RNA drugs, it will be important to develop a more sophisticated understanding of the genes and pathways that enhance or, in this case, block RNA delivery.

Our data suggest that metabolic signaling can alter LNP delivery in vivo in unexpected ways. We believe that these data constitute early steps toward an important goal: exploiting natural differences in cell signaling to improve cell type–specific nanoparticle delivery (*59*). That said, metabolism is broadly defined, and it is important to acknowledge that multiple mechanisms of action could be involved in the PIP3-induced phenotype we observe. Additional studies will be required to elucidate the complexity and extent of interaction between these multiple metabolic mechanisms as well as confirm that these mechanisms are conserved in vivo. Despite this, we eventually hope to identify signaling pathways that promote the activity of a therapeutic RNA in a target cell type while reducing its activity in off-target cells using high-throughput in vivo techniques such as single-cell RNA-seq (*60*).

It is important to acknowledge the limitations of this study. First, we were unable to identify the non-clathrin and non-caveolin pathways that were affected by PIP3. Our cell uptake and transcriptomic data also did not elucidate the extent to which endocytosis or endosomal escape were affected by PIP3. Second, our in vivo studies were in mice; future work will need to evaluate whether the same results are observed in other models, most notably NHPs. Similarly, given that in vitro experiments are often not representative of in vivo experiments, it is necessary to study the metabolic and transcriptomic profiles of cells affected by PIP3 in vivo. Despite these caveats, we believe that these data provide evidence that cellular metabolism affects nanoparticle delivery and, more generally, that cell metabolism needs to be considered when designing RNA therapies.

MATERIALS AND METHODS

Chemical synthesis

Microwave irradiations were performed using a Biotage Initiator. Thin-layer chromatography was performed on precoated silica Gel GF plates and visualized using $KMnO_4$ stains. ^{1}H–nuclear magnetic resonance (NMR) spectra were recorded at 400 MHz (Varian) using $CDCl_3$ with tetramethylsilane (TMS) or residual solvent as standard. ^{13}C-NMR spectra were recorded at 100 MHz (Varian) using $CDCl_3$ with TMS or residual solvent as standard. High-resolution mass spectra (HRMS) were recorded on a time-of-flight mass spectrometer by electrospray ionization (ESI). All other chemicals were obtained from commercial sources.

Synthesis of compound **3** (fig. S8) (*28*). Compound **1** (20 g, 41.9 mmol, 1 eq) was charged in a 100-ml flask, and trifluoroacetic acid (42 ml) was slowly added at 0°C. The reaction mixture was stirred at room temperature for 30 min. The solvent was evaporated under reduced pressure and the crude product was dissolved in *N*,*N*′-dimethylformamide (5 ml) before being added dropwise to pyridine (300 ml) at 0°C. The reaction mixture was stirred at room temperature overnight. Pyridine was evaporated under reduced pressure, and the remaining white solid was washed with EtOAc (3 × 100 ml). Intermediate **2** was used in the next step without further purification. To a degassed solution of **2** (8.4 g, 13.0 mmol, 1 eq) in AcOH (acetic acid)/DCM (dichloromethane) (1/1, 300 ml) was added Pd/C (10 weight %, 3.0 g). The reaction mixture was then degassed for 5 min with H_2 and stirred at room temperature under H_2 atmosphere overnight. After completion of the reaction, the reaction mixture was filtered over a Celite pad and washed with MeOH (methanol) (500 ml). The filtrate was concentrated under reduced pressure to obtain a crude yellow viscous oil. Precipitation of the crude with EtOAc (50 ml) followed by further EtOAc washes (3 × 50 ml) afforded compound **3** (4.8 g, 98% yield) as a white solid. ^{1}H NMR (400 MHz, D_2O) δ 1.38 to 1.52 (m, 4H, CH2), 1.73 to 1.65 (m, 4H, CH2), 1.83 to 1.89 (m, 4H, CH2), 2.98 (t, J = 7.6 Hz, 4H, NCH2), 4.14 (t, J = 5.2 Hz, 2H, COCH). ^{13}C NMR (100 MHz, D_2O) δ 21.0, 23.2, 26.3, 32.8, 39.0, 54.1, 170.2. HRMS [ESI, mass/charge ratio (*m*/*z*)] $C_{12}H_{25}N_4O_2$ $[M + H]^+$ calculated 257.1972, found 257.1968.

Synthesis of compound **cKK-E12** (fig. S8) (*28*). To a solution of **3** (84 mg, 0.22 mmol, 1 eq) and 1,2-epoxydodecane (247 mg, 1.34 mmol, 6 eq) in EtOH (ethanol) (2 ml) was added triethylamine (0.12 ml, 0.88 mmol, 4 eq) before being stirred for 30 min at room temperature. The reaction mixture was then irradiated in the microwave reactor at 150°C for 5 hours. After completion of the reaction, the reaction mixture was evaporated under reduced pressure and purified via flash column chromatography (silica gel, gradient eluent: 1 to 2.0% of MeOH/DCM then 2.0 to 4.0% MeOH/DCM containing 0.5% NH_4OH), affording **cKK-E12** (148 mg, 67%) as a light-yellow oil. ^{1}H NMR (400 MHz, $CDCl_3$) δ 0.87 (t, J = 6.8 Hz, 12 H, CH3), 1.21 to 1.35 (m, 64 H, CH_2), 1.37 to 1.65 (m, 16 H, CH_2), 1.71 to 1.95 (m, 4 H, CH_2), 2.19 to 2.66 (br, 12 H, NCH_2), 3.62 (m, 4 H, CHOH), 3.99 (m, 2 H, COCH). HRMS (ESI, *m*/*z*) $C_{60}H_{121}N_4O_6$ $[M + H]^+$ calculated 993.9281, found 993.9269.

Nanoparticle formulation

Nanoparticles were formulated in a microfluidic device as previously described (*26*) by mixing a nucleic acid, an ionizable lipid, polyethylene glycol (PEG), cholesterol, and a phospholipid. Nanoparticles were made with variable mole ratios of these constituents. The mass ratios for all the constituents were as follows: RNA was 7.5:1 for LNP1 and 10:1 for LNP2. LNP1 consisted of the ionizable lipid **cKK-E12**, cholesterol (Avanti Lipids, 700000P), C_{14}PEG2K (Avanti Lipids, 880150P), and DOTAP (Avanti Lipids, 890890P) or NBD-DOTAP (Avanti Lipids, 810890P). LNP2 consisted of the ionizable lipid 7C1, cholesterol, C_{14}PEG2K, and DOPE (Avanti Lipids, 850725P). LNP3 consisted of the ionizable lipid **cKK-E12**, cholesterol, C_{18}PEG2K (Avanti Lipids, 880120P), and DOPE (Avanti Lipids, 850725P) or AF647-DOPE (Millipore-Sigma, 42247). Chemically modified mRNA (GFP or Cre) was purchased from TriLink. The mRNA was diluted in 10 mM citrate buffer (Teknova) and loaded into a syringe (Hamilton Company). The materials making up the nanoparticle (**cKK-E12** or 7C1, cholesterol, PEG, and DOPE or DOTAP) were

diluted in 100% ethanol and loaded into a second syringe. The citrate phase and ethanol phase were mixed together in a microfluidic device using syringe pumps.

Nanoparticle characterization

LNP Z-average hydrodynamic diameter was measured using dynamic light scattering (Wyatt Technologies). LNPs were diluted in sterile 1× PBS to a concentration of ~0.06 μg/ml and analyzed. LNPs were used if they met three criteria: diameter > 20 nm, diameter < 200 nm, and autocorrelation function with only one inflection point. Particles that met these criteria were dialyzed in 1× PBS (Invitrogen) and sterile-filtered with a 0.22-μm filter.

Animal experiments

All animal experiments were performed in accordance with the Georgia Institute of Technology's Institutional Animal Care and Use Committee. C57BL/6J (#000664) and Ai14 LSL-Tomato (#007914) mice were purchased from the Jackson Laboratory. In all experiments, mice were aged 5 to 8 weeks, and $N = 3$ to 4 mice per group were intravenously injected via the lateral tail vein.

Nanoparticle and PIP3 dosing

Mice were injected with a total Cre mRNA (TriLink) dose of 1.0 mg/kg and a PIP3 (Cayman Chemical) dose of 10 mg/kg. RNA concentration was determined using NanoDrop (Thermo Scientific).

Cell culture

In vitro experiments were performed with mouse aortic endothelial cells (iMAECs, provided by H. Jo at Emory) (*29*), HEK cells (HEK293, GenTarget), iMAECs stably transduced with CAG-SpCas9–enhanced GFP, produced in the Dahlman Lab, or mouse aortic endothelial cells (C57E κB-GFP) (provided by M. Schwartz at Yale). In all cases, cells were maintained at 37°C and 5% CO_2 and cultured using previously established conditions. In all cases, cell media was supplemented by penicillin-streptomycin [penicillin G (500 U/ml) and streptomycin (0.5 mg/ml)] (PenStrep, VWR) and 10% (v/v) fetal bovine serum (FBS; VWR). HEKs were passaged with Dulbecco's modified Eagle's medium (DMEM) F-12 50/50 (Corning). iMAECs were passaged using DMEM with glucose (1 g/liter), L-glutamine, and sodium pyruvate (Corning), supplemented by 1% (v/v) MEM nonessential amino acid solution (MEMNEAA, Sigma-Aldrich) and endothelial cell growth supplement (25 μg/ml; EMD Millipore). C57E κB-GFP was passaged with EGM-2 media (Lonza).

Unless otherwise noted, cells were seeded in a 24-well plate at a density of 40,000 cells per well with 500 μl of media per well. Twenty-four hours later, LNPs were added with a total RNA dose of 50, 150, or 250 ng per well. Initial experiments done with L2K used a total RNA dose of 400 ng per well.

MTT assay

Cells were seeded in a 96-well plate at a cell density of 25,000 cells per well with 100 μl of media per well. Twenty-four hours later, PIP3 was added at a dose of 0, 10 or 20 μM. Six or 24 hours later, media was discarded and replaced with 50 μl of serum-free media (same as described above, without FBS) and 50 μl of MTT reagent (Abcam). Cells were incubated for 3 hours at 37°C and treated with 150 μl of MTT solvent (Abcam). Plates were then shaken for 15 min at 350 rpm. Formazan formation was quantified by measuring absorbance at optical density (OD) = 590 nm using a BioTek Synergy HTX Multi-Mode Microplate Reader.

LDH assay

Cells were seeded in a 96-well plate at a cell density of 10,000 cells per well with 100 μl of media per well. Twenty-four hours later, PIP3 was added at a dose of 0, 10, or 20 μM. The positive control received 12 μl of CytoScan LDH Lysis Buffer (G Biosciences). Twenty-four hours later, 50 μl of supernatant and 50 μl of the CytoScan LDH Assay Buffer (G Biosciences) were mixed together and incubated for 30 min at 37°C. Fifty microliters of CytoScan LDH Stop Solution (G Biosciences) was then added to the solution, and absorbance was measured at OD = 490 nm using a BioTek Synergy HTX Multi-Mode Microplate Reader.

NF-κB assay

C57E cells isolated from WT C57bl/6 aorta endothelium and immortalized with a py-MT lentiviral plasmid were used. Cells contain an NF-κB binding sequence upstream of a GFP reporter gene in their genome. The cells containing this construct constitutively express red fluorescent protein and only express GFP when NF-κB is released from its receptor protein [inhibitor of NF-κB (IκB-α)]. Cells were seeded in a 24-well plate at a density of 40,000 cells per well with 500 μl of media per well. Twenty-four hours later, PIP3 was added at a dose of 0, 10, or 20 μM. The positive control received 100 ng of LPS. Eight and 12 hours later, cells were analyzed via flow cytometry using a BD Accuri C6 Benchtop Flow Cytometer (fig. S1, H to J).

Fixed-cell staining

Cells were plated in glass-bottom 24-well plates at a density of 40,000 cells per well 1 day before LNP delivery. Cells were fixed 6 or 24 hours after transfection with 4% paraformaldehyde (Electron Microscopy Sciences) for 10 min at room temperature before permeabilization with 0.2% Triton X-100 (Sigma-Aldrich) for 5 min at room temperature. To stain for endosomes, cells were first blocked for nonspecific binding with 5% bovine serum albumin (Sigma-Aldrich) for 30 min at 37°C and then incubated with a mixture of anti-Rab7 (Invitrogen), anti-EEA1 (Invitrogen), and anti-CD63 (Abcam) for 30 min at 37°C. Cells were then incubated with an Alexa Fluor 568 secondary antibody (Invitrogen) for 30 min at 37°C. Nuclei were stained with 4′,6-diamidino-2-phenylindole (DAPI) (Life Technologies), and coverslips were placed over the cells in the dish and mounted with ProLong Gold (Life Technologies).

Microscopy

Images were acquired with a Hamamatsu Flash 4.0 v2 scientific complementary metal-oxide semiconductor camera on a PerkinElmer UltraView spinning disk confocal microscope mounted to a Zeiss Axiovert 200M body with a 63× numerical aperture 1.4 plan-apochromat objective. Images were acquired with Volocity acquisition software (PerkinElmer). All images were linearly contrast-enhanced. Colocalization analysis was performed via Volocity acquisition software by calculating the M1 and M2 coefficients for 30 to 40 cells per condition on unenhanced images.

Metabolomics

Metabolomics was performed for five groups (0 hours no PIP3, 6 hours no PIP3, 6 hours PIP3, 24 hours no PIP3, and 24 hours PIP3). Cells were seeded in six-well plates at 500,000 cells per well and cultured

for 24 hours before the start of the experiment. Four samples per time point and condition were created, with a fifth sample created for DNA quantification. Specifically, each replicate was created from two wells in different plates treated with the same condition. Cells were manually counted with a hemocytometer to check approximate number and viability. Methanol-based metabolite extraction was performed at each time point with −80°C methanol added to each sample before subsequent storage at −20°C until analysis. Methanol-based extraction preserves polar metabolites, a standard in cell-based metabolic extraction (*61*). The fifth sample was treated by aspirating all PBS and adding digestion buffer consisting of 1× tris-EDTA and proteinase K. Internal standards for each sample were added based on cell number. Cell counting was performed on the fifth sample collected for each condition via the Promega Quant-iT PicoGreen method using pico-green dye reagent and Promega fluorescent plate reader to quantify double-stranded DNA concentration as according to the manufacturer's protocol.

Internal standards of ribitol and ^{13}C-glucose were added to the methanol-extracted samples in concentrations of 1 μl per 1×10^6 cells and 2 μl per 1×10^6 cells, respectively, and then dried in a speed vacuum system (Savant SpeedVac SPD1030) overnight at 45°C and 5.1 mtorr. After drying, samples consisted of only a dehumidified pellet of extracted metabolites and were stored at −80°C.

Sample derivatization procedure was performed as described previously (*61*). Briefly, addition of the derivatizing agent methoxyamine (added alone for 1.5 hours) and then further addition of *N*-methyl-*N*-(trimethylsilyl)-trifluoroacetamide (MSTFA) (6 hours) was performed for samples and then placed into vials loaded to the gas chromatography–mass spectrometry (GCMS) system (Shimadzu GCMS QP2010 ultra). No samples were left in derivatizing agents more than 22 hours, as this has been shown to degrade the metabolites present (*62*). The GCMS performed for 1 hour runs with a linear heating regime of the GC column from 70° to 310°C.

Bioinformatics analysis for metabolomics

Data were collected on the GCMS postrun analysis software (Shimadzu). Raw data containing the peak intensities were compared to a preexisting custom-built library of metabolites containing 74 metabolites found within mammalian cell metabolism. This produced peak areas present for each of these metabolites. The peak areas of each run were normalized to area of the ribitol peak, one of the internal standards added. As per the previous section, this normalization procedure provides a method to normalize metabolite peak areas. The ribitol peak areas were consistent within <1% variation across all runs of each sample, an indication of run consistency and equipment accuracy. The ratios of the two ^{13}C-glucose derivatives (second internal standard added) were taken for each run. For each run, if the ratio was greater than 1 SD away from the average ratio of all runs in that sample, the run was removed. This ensured that peak area values were statistically consistent between runs. Metabolites with a coefficient of variation greater than 25% across remaining runs for each sample were also removed. The average of each metabolite across all runs in a sample was calculated to be the effective metabolite presence in the original sample. The final data contained a single value for metabolite presence in each sample—four samples per condition and time point.

Statistical analysis was performed on the data through dimensionality reduction techniques and significance analysis. No additional data cleaning was performed specifically for any of these techniques. PCA and hierarchical clustering were performed in R and visualized using ggplot2 and heatplot packages. PCA considered three PCs, covering only >50% of observed variance in the data; this indicates that the data were variable in a large number of dimensions (metabolites). Identification of significantly up- and down-regulated metabolites between two groups was performed using the method of significance analysis of microarrays (SAM) as described previously (*63*), implemented using the SAMR package in R. The delta value for SAM was calculated using the latest method described in the SAMR release documentation. Comparisons of metabolites between the PIP3-containing and non–PIP3-containing groups at 6 and 24 hours were compared and mapped to box plots and pathway maps for visualization and further analysis.

Whole-transcriptome sequencing

iMAECs were seeded in a six-well plate at a seeding density of 500,000 cells per well. Cells were cultured for 24 hours as written above and then treated with 10 μM PIP3 or no PIP3. Six or 24 hours later, RNA was harvested from the cells. Total RNA was extracted using the RNeasy Mini Kit (Qiagen) following the manufacturer's protocol. The quantity and quality of RNA were examined by the Qubit RNA High Sensitivity Assay Kit, Qubit 3.0 Fluorometer (Life Technologies), and Agilent 2100 Bioanalyzer (Agilent Technologies). High-quality RNA (1 μg) from each sample was used for cDNA synthesis and sequencing, using the TruSeq Stranded mRNA protocol from Illumina (Illumina Inc.). After generating the clusters, library sequencing was performed on an Illumina NextSeq platform to create paired-end reads with a length of 75 base pairs.

Bioinformatics analysis for RNA-seq

The sequenced reads were trimmed and aligned to the mouse genome (mm10) using Isas analysis software 3.19.1.12, SAMtools 0.1.20, STAR aligner STAR_2.6.1a, Salmon quantification software 0.11.2, and Strelka Variant Calling software 2.9.9. Differential expression analysis was determined using DESeq2 (*64*). Only genes with an adjusted *P* value (false discovery rate) or less than 0.05 and a fold change greater than 1.5 were included within the subsequent GO and KEGG pathway analysis. To understand the functions of the differentially expressed genes, GO functional enrichment and KEGG pathway analysis were carried out by the Enrichr web server (*65*) and KEGGMapper (www.kegg.jp/), respectively.

Cell isolation and staining

Mice were euthanized 3 days after administration of LNPs and immediately perfused with 20 ml of 1× PBS through the right atrium. In all cases, the lung, liver, and spleen were isolated following perfusion. All tissues were finely minced with micro dissecting scissors and then placed in a 1× PBS solution containing collagenase type I (450 U/ml) (Sigma-Aldrich), collagenase XI (125 U/ml) (Sigma-Aldrich), and hyaluronidase (60 U/ml) (Sigma-Aldrich) at 37°C and 750 rpm for 45 min. The digestive enzyme for spleen included collagenase IV (10 mg/ml) (Sigma-Aldrich) (*66*). Digested tissues were passed through a 70-μm filter, and red blood cells were lysed with red blood cell lysis buffer (Alfa Aesar). Cells were stained to identify specific cell populations, and flow cytometry was performed using a BD FacsFusion cell analyzer. Antibody clones used were anti-CD31 (390, BioLegend), anti-CD45.2 (104, BioLegend), anti-CD11b (M1/70, BioLegend), anti-CD68 (FA-11, BioLegend), and anti-CD47 (miap301, BioLegend). Phycoerythrin-conjugated anti-CD47 was

used as a compensation control for tdTomato when running flow cytometry for in vivo experiments. Representative gating strategies for liver, lung, and spleen populations using control Ai14 mice injected with PBS are included in fig. S9 (A to F).

Statistical analysis

Unless otherwise noted, statistical analyses were done using GraphPad Prism 8. Unless otherwise noted, data are plotted as means ± SEM. As indicated in each figure caption, an unpaired *t* test, one-way analysis of variance (ANOVA), or two-way ANOVA was used to analyze the data.

SUPPLEMENTARY MATERIALS

Supplementary material for this article is available at http://advances.sciencemag.org/cgi/content/full/6/30/eaba5672/DC1

REFERENCES AND NOTES

1. F. Wang, L. Yu, M. P. Monopoli, P. Sandin, E. Mahon, A. Salvati, K. A. Dawson, The biomolecular corona is retained during nanoparticle uptake and protects the cells from the damage induced by cationic nanoparticles until degraded in the lysosomes. *Nanomedicine* **9**, 1159–1168 (2013).
2. A. Salvati, A. S. Pitek, M. P. Monopoli, K. Prapainop, F. B. Bombelli, D. R. Hristov, P. M. Kelly, C. Åberg, E. Mahon, K. A. Dawson, Transferrin-functionalized nanoparticles lose their targeting capabilities when a biomolecule corona adsorbs on the surface. *Nat. Nanotechnol.* **8**, 137–143 (2013).
3. T. Cedervall, I. Lynch, S. Lindman, T. Berggård, E. Thulin, H. Nilsson, K. A. Dawson, S. Linse, Understanding the nanoparticle-protein corona using methods to quantify exchange rates and affinities of proteins for nanoparticles. *Proc. Natl. Acad. Sci. U.S.A.* **104**, 2050–2055 (2007).
4. A. Akinc, W. Querbes, S. De, J. Qin, M. Frank-Kamenetsky, K. N. Jayaprakash, M. Jayaraman, K. G. Rajeev, W. L. Cantley, J. R. Dorkin, J. S. Butler, L. Qin, T. Racie, A. Sprague, E. Fava, A. Zeigerer, M. J. Hope, M. Zerial, D. W. Y. Sah, K. Fitzgerald, M. A. Tracy, M. Manoharan, V. Koteliansky, A. Fougerolles, M. A. Maier, Targeted delivery of RNAi therapeutics with endogenous and exogenous ligand-based mechanisms. *Mol. Ther.* **18**, 1357–1364 (2010).
5. D. Adams, A. Gonzalez-Duarte, W. D. O'Riordan, C.-C. Yang, M. Ueda, A. V. Kristen, I. Tournev, H. H. Schmidt, T. Coelho, J. L. Berk, K.-P. Lin, G. Vita, S. Attarian, V. Planté-Bordeneuve, M. M. Mezei, J. M. Campistol, J. Buades, T. H. Brannagan III, B. J. Kim, J. Oh, Y. Parman, Y. Sekijima, P. N. Hawkins, S. D. Solomon, M. Polydefkis, P. J. Dyck, P. J. Gandhi, S. Goyal, J. Chen, A. L. Strahs, S. V. Nochur, M. T. Sweetser, P. P. Garg, A. K. Vaishnaw, J. A. Gollob, O. B. Suhr, Patisiran, an RNAi therapeutic, for hereditary transthyretin amyloidosis. *N. Engl. J. Med.* **379**, 11–21 (2018).
6. S. Patel, N. Ashwanikumar, E. Robinson, A. DuRoss, C. Sun, K. E. Murphy-Benenato, C. Mihai, Ö. Almarsson, G. Sahay, Boosting intracellular delivery of lipid nanoparticle-encapsulated mRNA. *Nano Lett.* **17**, 5711–5718 (2017).
7. A. Akinc, G. Battaglia, Exploiting endocytosis for nanomedicines. *Cold Spring Harb. Perspect. Biol.* **5**, a016980 (2013).
8. J. Voigt, J. Christensen, V. P. Shastri, Differential uptake of nanoparticles by endothelial cells through polyelectrolytes with affinity for caveolae. *Proc. Natl. Acad. Sci. U.S.A.* **111**, 2942–2947 (2014).
9. J. Gilleron, W. Querbes, A. Zeigerer, A. Borodovsky, G. Marsico, U. Schubert, K. Manygoats, S. Seifert, C. Andree, M. Stöter, H. Epstein-Barash, L. Zhang, V. Koteliansky, K. Fitzgerald, E. Fava, M. Bickle, Y. Kalaidzidis, A. Akinc, M. Maier, M. Zerial, Image-based analysis of lipid nanoparticle-mediated siRNA delivery, intracellular trafficking and endosomal escape. *Nat. Biotechnol.* **31**, 638–646 (2013).
10. A. Wittrup, A. Ai, X. Liu, P. Hamar, R. Trifonova, K. Charisse, M. Manoharan, T. Kirchhausen, J. Lieberman, Visualizing lipid-formulated siRNA release from endosomes and target gene knockdown. *Nat. Biotechnol.* **33**, 870–876 (2015).
11. C. D. Sago, M. P. Lokugamage, G. N. Lando, N. Djeddar, N. N. Shah, C. Syed, A. V. Bryksin, J. E. Dahlman, Modifying a commonly expressed endocytic receptor retargets nanoparticles in vivo. *Nano Lett.* **18**, 7590–7600 (2018).
12. K. Paunovska, C. J. Gil, M. P. Lokugamage, C. D. Sago, M. Sato, G. N. Lando, M. Gamboa Castro, A. V. Bryksin, J. E. Dahlman, Analyzing 2000 in vivo drug delivery data points reveals cholesterol structure impacts nanoparticle delivery. *ACS Nano* **12**, 8341–8349 (2018).
13. M. Maugeri, M. Nawaz, A. Papadimitriou, A. Angerfors, A. Camponeschi, M. Na, M. Hölttä, P. Skantze, S. Johansson, M. Sundqvist, J. Lindquist, T. Kjellman, I. L. Martensson, T. Jin, P. Sunnerhagen, S. Östman, L. Lindfors, H. Valadi, Linkage between endosomal escape of LNP-mRNA and loading into EVs for transport to other cells. *Nat. Commun.* **10**, 4333 (2019).
14. A. C. Anselmo, S. Mitragotri, Nanoparticles in the clinic: An update. *Bioeng. Transl. Med.* **4**, e10143 (2019).
15. G. F. Lewis, D. J. Rader, New insights into the regulation of HDL metabolism and reverse cholesterol transport. *Circ. Res.* **96**, 1221–1232 (2005).
16. R. Kuai, D. Li, Y. E. Chen, J. J. Moon, A. Schwendeman, High-density lipoproteins (HDL)—Nature's multifunctional nanoparticles. *ACS Nano* **10**, 3015–3041 (2016).
17. C. N. Antonescu, T. E. McGraw, A. Klip, Reciprocal regulation of endocytosis and metabolism. *Cold Spring Harb. Perspect. Biol.* **6**, a016964 (2014).
18. W. Palm, C. B. Thompson, Nutrient acquisition strategies of mammalian cells. *Nature* **546**, 234–242 (2017).
19. J. Ochaba, A. F. Powers, K. A. Tremble, S. Greenlee, N. M. Post, J. E. Matson, A. R. MacLeod, S. Guo, M. Aghajan, A novel and translational role for autophagy in antisense oligonucleotide trafficking and activity. *Nucleic Acids Res.* **47**, 11284–11303 (2019).
20. W. S. Park, W. D. Heo, J. H. Whalen, N. A. O'Rourke, H. M. Bryan, T. Meyer, M. N. Teruel, Comprehensive identification of PIP3-regulated PH domains from *C. elegans* to *H. sapiens* by model prediction and live imaging. *Mol. Cell* **30**, 381–392 (2008).
21. C. C. Dibble, L. C. Cantley, Regulation of mTORC1 by PI3K signaling. *Trends Cell Biol.* **25**, 545–555 (2015).
22. I. Vivanco, C. L. Sawyers, The phosphatidylinositol 3-kinase AKT pathway in human cancer. *Nat. Rev. Cancer* **2**, 489–501 (2002).
23. V. Laketa, S. Zarbakhsh, A. Traynor-Kaplan, A. Macnamara, D. Subramanian, M. Putyrski, R. Mueller, A. Nadler, M. Mentel, J. Saez-Rodriguez, R. Pepperkok, C. Schultz, PIP_3 induces the recycling of receptor tyrosine kinases. *Sci. Signal.* **7**, ra5 (2014).
24. I. C. Fields, S. M. King, E. Shteyn, R. S. Kang, H. Fölsch, Phosphatidylinositol 3,4,5-trisphosphate localization in recycling endosomes is necessary for AP-1B-dependent sorting in polarized epithelial cells. *Mol. Biol. Cell* **21**, 95–105 (2010).
25. N. Hay, The Akt-mTOR tango and its relevance to cancer. *Cancer Cell* **8**, 179–183 (2005).
26. D. Chen, K. T. Love, Y. Chen, A. A. Eltoukhy, C. Kastrup, G. Sahay, A. Jeon, Y. Dong, K. A. Whitehead, D. G. Anderson, Rapid discovery of potent siRNA-containing lipid nanoparticles enabled by controlled microfluidic formulation. *J. Am. Chem. Soc.* **134**, 6948–6951 (2012).
27. K. J. Kauffman, M. A. Oberli, J. R. Dorkin, J. E. Hurtado, J. C. Kaczmarek, S. Bhadani, J. Wyckoff, R. Langer, A. Jaklenec, D. G. Anderson, Rapid, single-cell analysis and discovery of vectored mRNA transfection in vivo with a loxP-flanked tdTomato reporter mouse. *Mol. Ther. Nucleic Acids* **10**, 55–63 (2018).
28. Y. Dong, K. T. Love, J. R. Dorkin, S. Sirirungruang, Y. Zhang, D. Chen, R. L. Bogorad, H. Yin, Y. Chen, A. J. Vegas, C. A. Alabi, G. Sahay, K. T. Olejnik, W. Wang, A. Schroeder, A. K. Lytton-Jean, D. J. Siegwart, A. Akinc, C. Barnes, S. A. Barros, M. Carioto, K. Fitzgerald, J. Hettinger, V. Kumar, T. I. Novobrantseva, J. Qin, W. Querbes, V. Koteliansky, R. Langer, D. G. Anderson, Lipopeptide nanoparticles for potent and selective siRNA delivery in rodents and nonhuman primates. *Proc. Natl. Acad. Sci. U.S.A.* **111**, 3955–3960 (2014).
29. C.-W. Ni, S. Kumar, C. J. Ankeny, H. Jo, Development of immortalized mouse aortic endothelial cell lines. *Vascul. Cell* **6**, 7 (2014).
30. C. D. Sago, M. P. Lokugamage, K. Paunovska, D. A. Vanover, C. M. Monaco, N. N. Shah, M. G. Castro, S. E. Anderson, T. G. Rudoltz, G. N. Lando, P. M. Tiwari, J. L. Kirschman, N. Willett, Y. C. Jang, P. J. Santangelo, A. V. Bryksin, J. E. Dahlman, High-throughput in vivo screen of functional mRNA delivery identifies nanoparticles for endothelial cell gene editing. *Proc. Natl. Acad. Sci. U.S.A.* **115**, E9944–E9952 (2018).
31. J. E. Dahlman, C. Barnes, O. F. Khan, A. Thiriot, S. Jhunjunwala, T. E. Shaw, Y. Xing, H. B. Sager, G. Sahay, L. Speciner, A. Bader, R. L. Bogorad, H. Yin, T. Racie, Y. Dong, S. Jiang, D. Seedorf, A. Dave, K. Singh Sandhu, M. J. Webber, T. Novobrantseva, V. M. Ruda, K. R. Lytton-JeanAbigail, C. G. Levins, B. Kalish, D. K. Mudge, M. Perez, L. Abezgauz, P. Dutta, L. Smith, K. Charisse, M. W. Kieran, K. Fitzgerald, M. Nahrendorf, D. Danino, R. M. Tuder, U. H. von Andrian, A. Akinc, D. Panigrahy, A. Schroeder, V. Koteliansky, R. Langer, D. G. Anderson, *In vivo* endothelial siRNA delivery using polymeric nanoparticles with low molecular weight. *Nat. Nanotechnol.* **9**, 648–655 (2014).
32. O. F. Khan, P. S. Kowalski, J. C. Doloff, J. K. Tsosie, V. Bakthavatchalu, C. B. Winn, J. Haupt, M. Jamiel, R. Langer, D. G. Anderson, Endothelial siRNA delivery in nonhuman primates using ionizable low-molecular weight polymeric nanoparticles. *Sci. Adv.* **4**, eaar8409 (2018).
33. M. P. Lokugamage, Z. Gan, C. Zurla, J. Levin, F. Z. Islam, S. Kalathoor, M. Sato, C. D. Sago, P. J. Santangelo, J. E. Dahlman, Mild innate immune activation overrides efficient nanoparticle-mediated RNA delivery. *Adv. Mater.* **32**, 1904905 (2020).
34. C. Wang, E. de Jong, K. A. Sjollema, I. S. Zuhorn, Entry of PIP3-containing polyplexes into MDCK epithelial cells by local apical-basal polarity reversal. *Sci. Rep.* **6**, 21436 (2016).
35. H. T. McMahon, E. Boucrot, Molecular mechanism and physiological functions of clathrin-mediated endocytosis. *Nat. Rev. Mol. Cell Biol.* **12**, 517–533 (2011).
36. P. A. Orlandi, P. H. Fishman, Filipin-dependent inhibition of cholera toxin: Evidence for toxin internalization and activation through caveolae-like domains. *J. Cell Biol.* **141**, 905–915 (1998).
37. J. L. Kirschman, S. Bhosle, D. Vanover, E. L. Blanchard, K. H. Loomis, C. Zurla, K. Murray, B. C. Lam, P. J. Santangelo, Characterizing exogenous mRNA delivery, trafficking,

cytoplasmic release and RNA-protein correlations at the level of single cells. *Nucleic Acids Res.* **45**, e113 (2017).
38. S. D. Sommerfeld, C. Cherry, R. M. Schwab, L. Chung, D. R. Maestas Jr., P. Laffont, J. E. Stein, A. Tam, S. Ganguly, F. Housseau, J. M. Taube, D. M. Pardoll, P. Cahan, J. H. Elisseeff, Interleukin-36γ–producing macrophages drive IL-17–mediated fibrosis. *Sci. Immunol.* **4**, eaax4783 (2019).
39. F. Chen, A. Cao, S. Yao, H. L. Evans-Marin, H. Liu, W. Wu, E. D. Carlsen, S. M. Dann, L. Soong, J. Sun, Q. Zhao, Y. Cong, mTOR mediates IL-23 induction of neutrophil IL-17 and IL-22 production. *J. Immunol.* **196**, 4390–4399 (2016).
40. N. Moreno-Marín, J. M. Merino, A. Alvarez-Barrientos, D. P. Patel, S. Takahashi, J. M. González-Sancho, P. Gandolfo, R. M. Rios, A. Muñoz, F. J. Gonzalez, P. M. Fernández-Salguero, Aryl hydrocarbon receptor promotes liver polyploidization and inhibits PI3K, ERK, and Wnt/β-catenin signaling. *iScience* **4**, 44–63 (2018).
41. W. Ren, J. Yin, J. Duan, G. Liu, B. Tan, G. Yang, G. Wu, F. W. Bazer, Y. Peng, Y. Yin, mTORC1 signaling and IL-17 expression: Defining pathways and possible therapeutic targets. *Eur. J. Immunol.* **46**, 291–299 (2016).
42. H. Meng, X. Zhang, S. J. Lee, D. K. Strickland, D. A. Lawrence, M. M. Wang, Low density lipoprotein receptor-related protein-1 (LRP1) regulates thrombospondin-2 (TSP2) enhancement of Notch3 signaling. *J. Biol. Chem.* **285**, 23047–23055 (2010).
43. M. P. Czech, PIP2 and PIP3: Complex roles at the cell surface. *Cell* **100**, 603–606 (2000).
44. M. C. C. Gomes-Marcondes, M. J. Tisdale, Induction of protein catabolism and the ubiquitin-proteasome pathway by mild oxidative stress. *Cancer Lett.* **180**, 69–74 (2002).
45. Y. Jiang, J. Kou, X. Han, X. Li, Z. Zhong, Z. Liu, Y. Zheng, Y. Tian, L. Yang, ROS-dependent activation of autophagy through the PI3K/Akt/mTOR pathway is induced by hydroxysafflor yellow A-sonodynamic therapy in THP-1 macrophages. *Oxid. Med. Cell. Longev.* **2017**, 8519169 (2017).
46. R. R. V. Malapaka, S. Khoo, J. Zhang, J. H. Choi, X. E. Zhou, Y. Xu, Y. Gong, J. Li, E.-L. Yong, M. J. Chalmers, L. Chang, J. H. Resau, P. R. Griffin, Y. E. Chen, H. E. Xu, Identification and mechanism of 10-carbon fatty acid as modulating ligand of peroxisome proliferator-activated receptors. *J. Biol. Chem.* **287**, 183–195 (2012).
47. A. J. Kowaltowski, N. C. de Souza-Pinto, R. F. Castilho, A. E. Vercesi, Mitochondria and reactive oxygen species. *Free Radic. Biol. Med.* **47**, 333–343 (2009).
48. Y. Y. C. Lo, T. F. Cruz, Involvement of reactive oxygen species in cytokine and growth factor induction of *c-fos* expression in chondrocytes. *J. Biol. Chem.* **270**, 11727–11730 (1995).
49. G. Song, G. Ouyang, S. Bao, The activation of Akt/PKB signaling pathway and cell survival. *J. Cell. Mol. Med.* **9**, 59–71 (2005).
50. K. Paunovska, C. D. Sago, C. M. Monaco, W. H. Hudson, M. G. Castro, T. G. Rudoltz, S. Kalathoor, D. A. Vanover, P. J. Santangelo, R. Ahmed, A. V. Bryksin, J. E. Dahlman, A direct comparison of in vitro and in vivo nucleic acid delivery mediated by hundreds of nanoparticles reveals a weak correlation. *Nano Lett.* **18**, 2148–2157 (2018).
51. K. Paunovska, A. J. Da Silva Sanchez, C. D. Sago, Z. Gan, M. P. Lokugamage, F. Z. Islam, S. Kalathoor, B. R. Krupczak, J. E. Dahlman, Nanoparticles containing oxidized cholesterol deliver mRNA to the liver microenvironment at clinically relevant doses. *Adv. Mater.* **31**, e1807748 (2019).
52. N. Mizushima, M. Komatsu, Autophagy: Renovation of cells and tissues. *Cell* **147**, 728–741 (2011).
53. N. Mizushima, Autophagy: Process and function. *Genes Dev.* **21**, 2861–2873 (2007).
54. D. Gatica, V. Lahiri, D. J. Klionsky, Cargo recognition and degradation by selective autophagy. *Nat. Cell Biol.* **20**, 233–242 (2018).
55. K. K. Ray, U. Landmesser, L. A. Leiter, D. Kallend, R. Dufour, M. Karakas, T. Hall, R. P. T. Troquay, T. Turner, F. L. J. Visseren, P. Wijngaard, R. S. Wright, J. J. P. Kastelein, Inclisiran in patients at high cardiovascular risk with elevated LDL cholesterol. *N. Engl. J. Med.* **376**, 1430–1440 (2017).
56. J. L. S. Willoughby, A. Chan, A. Sehgal, J. S. Butler, J. K. Nair, T. Racie, S. Shulga-Morskaya, T. Nguyen, K. Qian, K. Yucius, K. Charisse, T. J. C. van Berkel, M. Manoharan, K. G. Rajeev, M. A. Maier, V. Jadhav, T. S. Zimmermann, Evaluation of GalNAc-siRNA conjugate activity in pre-clinical animal models with reduced asialoglycoprotein receptor expression. *Mol. Ther.* **26**, 105–114 (2018).
57. M. E. Østergaard, J. Yu, G. A. Kinberger, W. B. Wan, M. T. Migawa, G. Vasquez, K. Schmidt, H. J. Gaus, H. M. Murray, A. Low, E. E. Swayze, T. P. Prakash, P. P. Seth, Efficient synthesis and biological evaluation of 5'-GalNAc conjugated antisense oligonucleotides. *Bioconjug. Chem.* **26**, 1451–1455 (2015).
58. J. K. Nair, J. L. Willoughby, A. Chan, K. Charisse, M. R. Alam, Q. Wang, M. Hoekstra, P. Kandasamy, A. V. Kel'in, S. Milstein, N. Taneja, J. O'Shea, S. Shaikh, L. Zhang, R. J. van der Sluis, M. E. Jung, A. Akinc, R. Hutabarat, S. Kuchimanchi, K. Fitzgerald, T. Zimmermann, T. J. van Berkel, M. A. Maier, K. G. Rajeev, M. Manoharan, Multivalent *N*-acetylgalactosamine-conjugated siRNA localizes in hepatocytes and elicits robust RNAi-mediated gene silencing. *J. Am. Chem. Soc.* **136**, 16958–16961 (2014).
59. C. D. Sago, B. R. Krupczak, M. P. Lokugamage, Z. Gan, J. E. Dahlman, Cell subtypes within the liver microenvironment differentially interact with lipid nanoparticles. *Cell. Mol. Bioeng.* **12**, 389–397 (2019).
60. K. Paunovska, D. Loughrey, C. D. Sago, R. Langer, J. E. Dahlman, Using large datasets to understand nanotechnology. *Adv. Mater.* **31**, e1902798 (2019).
61. H. Kanani, P. K. Chrysanthopoulos, M. I. Klapa, Standardizing GC-MS metabolomics. *J. Chromatogr. B* **871**, 191–201 (2008).
62. H. H. Kanani, M. I. Klapa, Data correction strategy for metabolomics analysis using gas chromatography-mass spectrometry. *Metab. Eng.* **9**, 39–51 (2007).
63. V. G. Tusher, R. Tibshirani, G. Chu, Significance analysis of microarrays applied to the ionizing radiation response. *Proc. Natl. Acad. Sci. U.S.A.* **98**, 5116–5121 (2001).
64. M. I. Love, W. Huber, S. Anders, Moderated estimation of fold change and dispersion for RNA-seq data with DESeq2. *Genome Biol.* **15**, 550 (2014).
65. M. V. Kuleshov, M. R. Jones, A. D. Rouillard, N. F. Fernandez, Q. Duan, Z. Wang, S. Koplev, S. L. Jenkins, K. M. Jagodnik, A. Lachmann, M. G. McDermott, C. D. Monteiro, G. W. Gundersen, A. Ma'ayan, Enrichr: A comprehensive gene set enrichment analysis web server 2016 update. *Nucleic Acids Res.* **44**, W90–W97 (2016).
66. H. B. Sager, P. Dutta, J. E. Dahlman, M. Hulsmans, G. Courties, Y. Sun, T. Heidt, C. Vinegoni, A. Borodovsky, K. Fitzgerald, G. R. Wojtkiewicz, Y. Iwamoto, B. Tricot, O. F. Khan, K. J. Kauffman, Y. Xing, T. E. Shaw, P. Libby, R. Langer, R. Weissleder, F. K. Swirski, D. G. Anderson, M. Nahrendorf, RNAi targeting multiple cell adhesion molecules reduces immune cell recruitment and vascular inflammation after myocardial infarction. *Sci. Transl. Med.* **8**, 342ra80 (2016).

Acknowledgments: We thank M. Schwartz at Yale and S. Durham and the Georgia Tech Cellular Analysis and Cytometry Core. J.E.D. thanks T. Shaw. **Funding:** J.E.D. was funded by Georgia Tech startup funds and the NIH R01 GM132985. K.P. was funded by the NIH/NIGMS-sponsored Cell and Tissue Engineering (CTEng) Biotechnology Training Program (T32GM008433). E.L.B. was funded by the NSF (DGE-1650044). D.L. was funded by the Shurl and Kay Curci Foundation. **Author contributions:** K.P., A.D.S., M.T.F., D.L., A.M., and J.E.D. designed experiments. K.P. A.D.S., M.T.F., D.L., and J.E.D. performed the experiments with help from other authors. K.P., A.D.S., M.T.F., A.M., D.L., and J.E.D. analyzed the data. K.P., A.D.S., and J.E.D. wrote the paper with input from all authors. **Competing interests:** J.E.D. is a co-founder of Guide Therapeutics. The authors declare that they have no other competing interests. **Data and materials availability:** All data needed to evaluate the conclusions in the paper are present in the paper and/or the Supplementary Materials. Additional data related to this paper may be requested from the authors.

Submitted 20 December 2019
Accepted 5 June 2020
Published 22 July 2020
10.1126/sciadv.aba5672

Citation: K. Paunovska, A. Da Silva Sanchez, M. T. Foster, D. Loughrey, E. L. Blanchard, F. Z. Islam, Z. Gan, A. Mantalaris, P. J. Santangelo, J. E. Dahlman, Increased PIP3 activity blocks nanoparticle mRNA delivery. *Sci. Adv.* **6**, eaba5672 (2020).